



Investigating the Geotechnical Properties of the Lunar South Pole with NASA VIPER's Mobility System

Erin Rezich¹ , Valentin T. Bickel² , Parker L. Francis³, Arno Rogg⁴, Antoine Tardy⁴, Colin Creager¹, Heather A. Oravec⁵, Alexander Schepelmann¹ , Kimberly Ennico-Smith⁶ , Ariel Deutsch^{6,7} , and Masatoshi Hirabayashi⁸

¹ NASA Glenn Research Center, Cleveland, OH 44135, USA; erin.t.rezich@nasa.gov

² Center for Space and Habitability, University of Bern, 3012 Bern, Switzerland

³ NASA Johnson Space Center, Houston, TX 77058, USA

⁴ KBR, NASA Ames Research Center, Moffett Field, CA 94035, USA

⁵ The University of Akron, Akron, OH 44325, USA

⁶ NASA Ames Research Center, Moffett Field, CA 94035, USA

⁷ Bay Area Environmental Research Institute, Moffett Field, CA 94035, USA

⁸ Georgia Institute of Technology, Atlanta, GA 30332, USA

Received 2024 December 31; revised 2025 April 7; accepted 2025 April 23; published 2025 July 18

Abstract

The NASA Volatiles Investigating Polar Exploration Rover (VIPER) is capable of assessing the geotechnical properties of the lunar south pole's terrain, specifically as they pertain to terramechanics or the wheel–terrain interaction, combining the rover's mobility system and science payloads. This paper focuses on one key aspect of VIPER's mission: the quantitative evaluation of geotechnical parameters via tractive performance by analyzing wheel and wheel–regolith interaction dynamics. As VIPER navigates the largely uncharted terrain of the Moon's south pole, sophisticated onboard instrumentation will monitor and record detailed interactions between the rover's wheels, chassis, and the lunar surface. These measurements will capture critical data such as wheel slip and sinkage, offering insights into the mechanical behavior of the soil under actual lunar conditions. The findings from VIPER are expected to provide a foundational understanding of the lunar south pole's regolith mechanics, directly informing the design and navigation strategies of future lunar missions, including the deployment of more advanced rovers and crewed vehicles. By integrating lunar surface observations with the rover's kinematic model and understood terrestrial mobility performance, the study aims to enhance predictive accuracy regarding rover tractive performance over sloped, level, and potentially volatile-rich terrain. Ground truth geotechnical assessments and proceeding mobility characterization work will serve as a cornerstone for verifying and improving both terrestrial test approaches and simulation models that underpin mission planning and risk management for subsequent explorations.

Unified Astronomy Thesaurus concepts: [Lunar surface \(974\)](#); [Lunar regolith \(2315\)](#)

1. Introduction

The ability to properly assess the mobility performance of lunar rovers on Earth is key for informing design decisions, maturing technology, and ensuring mission success. However, due to the uncertainty of the lunar terrain (regolith) properties, and the differences in environmental conditions between the Moon and Earth, this has been an ongoing challenge for planetary rover development. Both laboratory test approaches (K. Skonieczny et al. 2016; C. Creager et al. 2017; P. Niksirat et al. 2020) and modeling approaches (V. S. Swamy et al. 2023; J. Kamohara et al. 2024) have been utilized to address aspects of these challenges, but concessions must be made for each methodology. Factors such as terrain properties, gravity, atmospheric conditions, and vehicle kinematics all have an impact on the performance of a rover, and no single approach can capture all of these. Full-scale rover development and verification testing cannot yet be done in lunar gravity; thus, approaches such as gravity off-loading, reduced mass test vehicles, or gravitational scaling laws (W. Hu et al. 2024) are implemented to mimic the correct contact pressure with the ground; but there are questions

as to the validity of these approaches. Similarly, it is not possible to simulate the effects of lunar gravity or vacuum on bulk lunar soil simulants during full-scale, Earth-based vehicle testing. Models and simulations can account for gravity but may not accurately capture the nuances of complex vehicle systems or tire-to-soil interactions. In addition, all of these approaches must make assumptions about the regolith properties, which are poorly constrained for the lunar south polar highlands terrain.

For decades, the missing piece needed to validate these methods has been ground-truth data from the lunar surface. Unfortunately, very little rover performance data exists from the surface of the Moon; the only relevant information are assessments of rover slope climbing and overall mobility performance from Apollo taken in the near-side equatorial mare regions (N. C. Costes et al. 1972; W. D. Carrier et al. 1991) and more recently that of the Yutu-2 rover's exploration of the far side of the moon, which informed slip ratio and regolith composition (L. Ding et al. 2022).

Since the Apollo era, various efforts attempted to characterize some of the geotechnical properties of the lunar regolith, but relatively large uncertainties remain in current estimations (A. L. Filice 1967; J. Eggleston et al. 1968; H. J. Moore 1970; H. J. Hovland & J. K. Mitchell 1973; V. T. Bickel et al. 2019; V. Bickel & D. Kring 2020; H. M. Sargeant et al. 2020).

The Volatiles Investigating Polar Exploration Rover (VIPER) mission (the VIPER rover illustrated in Figure 1)



Original content from this work may be used under the terms of the [Creative Commons Attribution 4.0 licence](#). Any further distribution of this work must maintain attribution to the author(s) and the title of the work, journal citation and DOI.

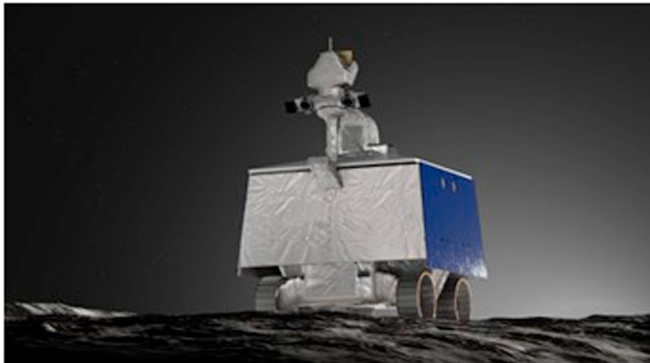


Figure 1. Rendering of VIPER on the lunar surface. The rover measures 2.5 m tall and 1.5 m in length and width.

presents a unique architecture to collect quantifiable rover performance data and characterize the geotechnical properties of the regolith at the south pole of the Moon, where most future lunar rovers and astronauts plan to traverse in the upcoming years as prescribed by the Artemis program (NASA 2020b). Ground-truth mobility performance data from the mission can be used to evaluate the existing test and simulation methodologies, either validating the approaches or providing information on how to improve their fidelity. Increased confidence in Earth-based rover test and simulation methodologies would greatly reduce risk for follow-on missions to the lunar south pole, such as the Lunar Terrain Vehicle, Pressurized Rover, or any proposed commercial rover missions.

2. Rover Systems Descriptions

The VIPER rover is a four-wheeled vehicle with a surface operations mass of 450 kg designed to traverse the lunar south pole. The primary scientific instrument payloads include The Regolith and Ice Drill for Exploration of New Terrains (TRIDENT; K. Zacny et al. 2025, in preparation, submitted this issue), the Neutron Spectrometer System (NSS; R. Elphic et al. 2025, in preparation, submitted this issue), the Near Infrared Volatiles Spectrometer System (NIRVSS; A. Colaprete et al. 2025a, in preparation, submitted this issue), and the Mass Spectrometer Observing Lunar Operations (MSolo; A. R. Aguilar et al. 2025, in preparation, submitted this issue). In addition, there is an array of cameras (L. Edwards et al. 2025, in preparation; R. Beyer et al. 2025, in preparation, submitted this issue) including two on the mast (NavCams) and two aft cameras (AftCams) for navigation, plus four cameras in the wheel wells (HazCams). In addition, the rover's Inertial Measurement Unit (IMU) can be used for gravimetry and seismological studies (K. Gansler et al. 2024). The rover's mobility system consists of four Wheel Modules attached to the chassis, the motor controllers that drive the active components in the Wheel Modules, and the flight software (FSW) that provides executive control.

Each Wheel Module, shown in Figure 2, consists of a rigid, groused (or lugged) wheel, a continuous rotation drive actuator, an independent steering actuator, and an independently actuated rigid suspension. Steering is configured with a range of motion such that omnidirectional course selection is available while maintaining maximum power input to the vehicle (i.e., when a Sun vector is bisecting the corner of the aft and port or starboard solar panels). The actuated suspension

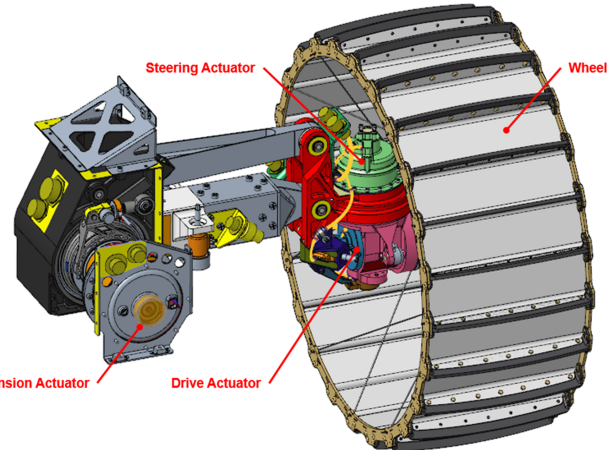


Figure 2. VIPER Wheel Module rendering with actuators denoted.

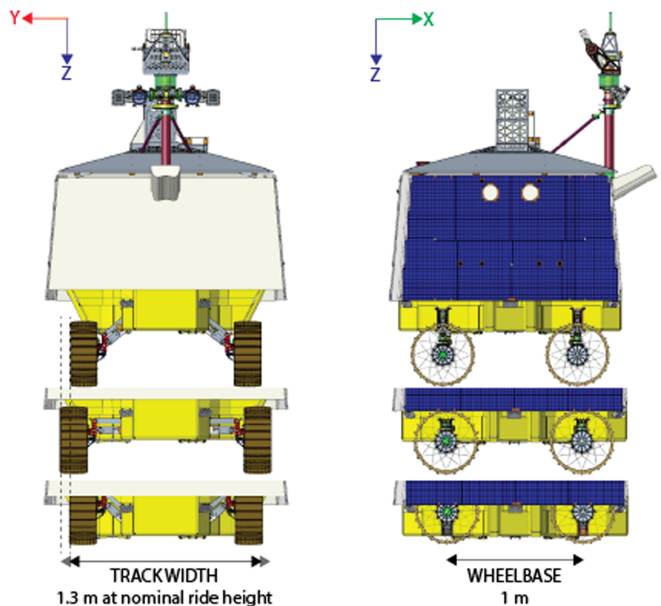


Figure 3. Illustration of wheelbase and track width parameters shown for three suspension ride height examples.

provides the vehicle with chassis stability control based on feedback from an onboard IMU, as well as wheel normal force control based on feedback from an integrated single axis torque transducer located within the suspension of each Wheel Module. The vehicle's track width is approximately 1.3 m at nominal ride height with a wheelbase of approximately 1 m. Both kinematic definitions are illustrated in Figure 3. Track width and wheelbase both vary slightly in different combined joint configurations due to the mobility system kinematics. Actuation of the suspension results in changes to the vehicle's ride height and track width, while actuation of the steering directly impacts both track width and wheelbase simultaneously.

VIPER's wheels, depicted in Figure 4, are 500 mm in diameter and 200 mm wide featuring 24 individual, crowned grousers each measuring 26 mm tall. The wheel diameter is measured to the grouser tip.

Design constraints based on the vehicle's mobility architecture and traction optimization had to be balanced in defining the wheel dimensions. Larger diameters typically result in

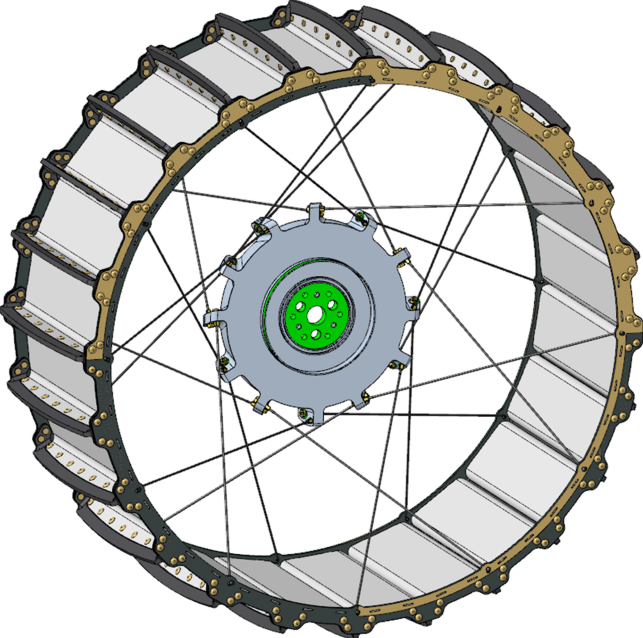


Figure 4. VIPER wheel with quadrature encoding metal finish pattern.

better performance (L. Ding et al. 2011), but have limitations due to collisions with chassis structure when steered. After various geometric trades were performed, the diameter and width were fixed, and the grouser count and height were optimized according to the methodology set out by K. Skonieczny et al. (2012).

The wheel is constructed of aluminum sheet metal rims and sidewalls, stainless steel spokes, and aluminum billet grousers and hub. The inboard face of the wheel rim is finished with a quadrature encoder pattern allowing for direct interpretation of wheel sinkage via HazCam imagery. Additionally, thorough testing in controlled environments both of an individual wheel and the full locomotion system have been completed to create a robust collection of performance and characterization data.

The drive actuator responsible for generating propulsive thrust in each Wheel Module is a brushless direct current (BLDC) motor coupled with a three-stage planetary gear set. Commutation and velocity control is provided by VIPER's motor controllers through resolver feedback on the motor shaft. Drive actuator effort (current) and velocity are critical measurements for establishing the wheel-regolith interaction seen by the vehicle at each wheel.

The steering actuator used to rotate the wheel in each Wheel Module is a BLDC motor coupled with a Harmonic Drive gear. The steering output can rotate between $+/-50^\circ$. For both steering and suspension actuators, commutation and velocity control are provided through resolver feedback on the motor shaft while output position control is closed with an additional output position resolver. Steering actuator effort (current) and resolver position are informative for complex traverses such as cross-slope driving where side slip and transverse loading are expected at the wheel-regolith interface. Furthermore, VIPER is often driven in a “crab” configuration, shown in Figure 5, where the traverse course is not aligned with the vehicle heading.

The suspension actuator comprises a BLDC motor coupled with a single-stage planetary gear set that further drives a Harmonic Drive gear. Between the gear stages, an exclusively



Figure 5. VIPER engineering unit demonstrating “crabbing” driving maneuver.

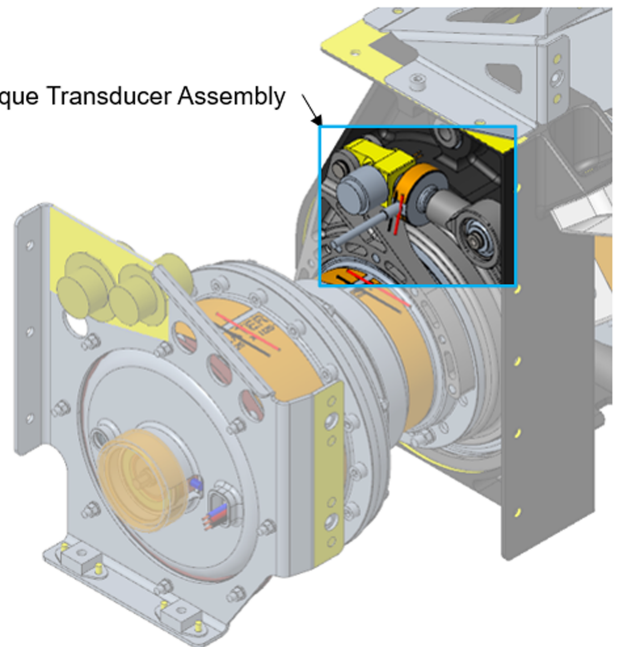


Figure 6. Suspension Assembly torque transducer.

mechanical antitackdrive device is present, which allows for powerless position holding. The joint output forms a four-bar linkage to the steering actuator, thus creating a quasilinear and parallel output motion from the rotary actuator. The suspension output has a range of motion providing a linear stroke of 360 mm.

VIPER's suspension actuator provides a unique measurement not previously available on other planetary rovers, which is a measured torque from within the Wheel Module used to estimate wheel normal force. A torque transducer, highlighted in Figure 6, is integrated into the mechanism design such that all torque produced or reacted about the joint is carried by the transducer. In cases where the suspension actuator is not accelerating, the torque transducer provides a direct measurement of wheel normal force. Some parasitic loads exist from the linkage and dust mitigation designs (e.g., wheel side loads and multilayer insulation tugging), but these effects can be

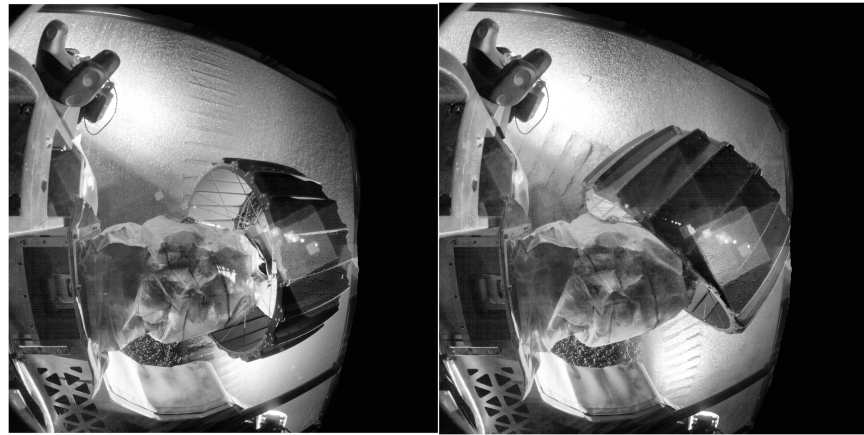


Figure 7. HazCam view of a wheel and tracks from the VIPER prototype vehicle, showcasing the front right wheel. The left image depicts the wheel in a straight position, while the right image shows the wheel steered at a 45° angle. The image has been processed using tone mapping based on Contrast Limited Adaptive Histogram Equalization (CLAHE) to enhance visibility. Note that the prototype camera used for this image has different distortion parameters than the flight configuration.

characterized and accounted for with some loss of measurement fidelity.

Each drive, steering, and suspension actuator is controlled by one of VIPER’s two Motor Controller (MC) assemblies. Each MC manages the complete input/output (I/O) and control for six actuators (i.e., two Wheel Module assemblies). The MC takes position or velocity commands from the flight software based on higher-level vehicle kinematic controllers. All actuator hardware level signals (resolver position/velocity, motor currents, etc.) are digitally converted, filtered, and consequently telemetered to the flight computer at a rate of 10 Hz. This telemetry rate will have a direct impact on the scientific fidelity of any terramechanics analyses; however, this rate is in-family with previous planetary rover telemetry (R. E. Arvidson et al. 2003). Some MC behaviors must be characterized with respect to hardware temperatures and accounted for in order to prevent loss of measurement fidelity.

VIPER is equipped with an IMU located near its geometric center. The unit, Northrup Grumman LN-200S, identical to the Curiosity’s IMU, provides linear acceleration and rotational velocity measurements of the vehicle’s chassis (K. Gansler et al. 2024). These measurements are valuable descriptors of the entire vehicle’s rigid body motion and, as such, feed directly into any terramechanics assessment. Furthermore, the lunar gravity vector can be deduced from the linear acceleration measurements.

A star tracker is mounted to VIPER’s zenith facing structure through the aft radiator panel. This external navigation reference provides the vehicle with a full attitude measurement. Changes in this measurement before and after a traverse can provide insight into yaw deviation experienced due to wheel–terrain interactions.

Image processing will be critical in assessing VIPER’s mobility performance characteristics including wheel沉降, vehicle forward velocity, and wheel slip. Unlike other data sources that provide only internal state information or single-point measurements of the rover’s interaction with the lunar environment, images collected by VIPER’s onboard cameras contain information about both the vehicle and the lunar surface, creating a holistic, information rich data source about the vehicle’s mobility performance on the Moon. Data sources and how information collected from various cameras on the

rover can be used to assess these performance characteristics are discussed below. VIPER’s hazard cameras (HazCams), aft cameras (AftCams), and navigation cameras (NavCams) are available on the rover to provide both context for other data sets as well as analysis of the driven track (L. Edwards et al. 2025, in preparation, submitted this issue; R. Beyer et al. 2025, in preparation, submitted this issue). The HazCams are oriented to look obliquely at each wheel, as shown in Figure 7. The AftCams are mounted to the body of the rover looking behind the vehicle, and the NavCams are mounted to the vehicle’s mast with pan and tilt capability.

The combination of resolvers, the IMU, and the star tracker is employed to generate position and attitude estimates of the VIPER rover. This is accomplished through the onboard Pose Estimation (PEST) software, which implements an extended Kalman Filter to consume the various measurements. While the suspension system has an influence on the exact position of the rover’s geometric center, the joint angles from the suspension are deliberately excluded from the PEST calculations. This decision is based on the potential noise that could arise from oscillations in the suspension, which would introduce unnecessary complexity and reduce the predictability of the system. Additionally, the impact of the suspension on overall position accuracy is considered minimal. For PEST calculations, only the steering and propulsion resolvers are utilized. During rover traverses, the orientation is determined using data from the IMU. The PEST software integrates the rover’s chassis velocity, derived from the kinematic model, to compute the rover’s X–Y surface position. This method provides an effective balance between simplicity and precision in determining the rover’s location during its operations.

2.1. Active Control Scheme

The mobility control system coordinates joint actuator motion into desired vehicle movements. VIPER’s control architecture involves a structured flow of commands through a waypoint controller, kinematic chain equations and suspension controllers, and joint-level control loops. The full architecture of the control loop and relevant sensors for feedback control can be seen in Figure 8.

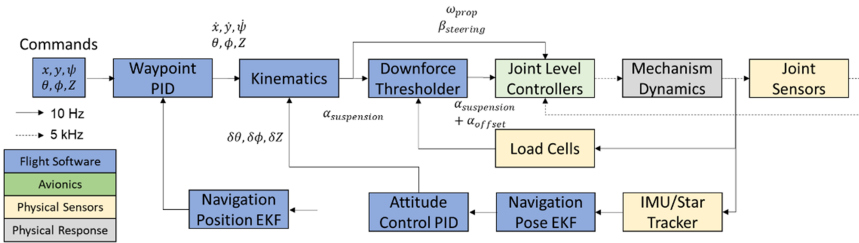


Figure 8. Diagram showing the integrated control scheme.

At the outermost level, waypoints at distances up to 10 m are commanded by ground operators. The onboard waypoint control loops make use of IMU and drive motor velocity feedback to move the vehicle along the straight-line trajectory. Turn-in-place motions occur at the beginning of each waypoint traverse to reorient the vehicle heading and steering actuators, as required. These turn-in-place motions steer the wheels into an “O” configuration and drive the wheels clockwise or counterclockwise with the intent to produce a yaw motion about the vehicle’s geometric center.

The kinematic chain equations operate within the waypoint loops and act as the mathematical backbone providing coordinated motion control between the twelve mobility actuators. Three kinematic flows exist within VIPER’s control architecture: Drive/Steering Inverse Kinematics (IK), Suspension Forward Kinematics (FK), and Suspension IK. The Drive/Steering IK processes desired chassis x -, y -, and yaw-velocities into coordinated drive velocities and steering angles. Additionally, this kinematic pairing prevents excessive wheel scrub by matching drive and steer velocities to the wheel–terrain interface (i.e., rolling the wheel while steering rather than dragging it). The Suspension FK converts suspension joint angles into kinematic pitch, roll, and average suspension height values. The Suspension IK processes kinematic pitch, roll, and average suspension height values into individual suspension joint angles.

The suspension control loops treat the suspension kinematic equations (and lower-level joint controllers) as a plant and provide attitude (kinematic pitch and roll), ground clearance, and downforce control. The Downforce Thresholding Controller is of specific interest to terramechanics investigations, as it adjusts individual suspension positions to maintain some selectable minimum normal force on the wheels derived from the torque transducer in the suspension. This loop is closed based on the suspension torque transducer telemetry. Additionally, the Attitude Controller adjusts all suspension positions simultaneously to satisfy a selectable pitch and roll with respect to gravity, based on the current pose estimate from PEST. In general, the VIPER mobility system operates with setpoints that place the vehicle chassis normal to the gravity vector. This results in improved slope climbing and passive obstacle traverse stability. Ground clearance monitoring provides saturation limiting to the commanded joint outputs to ensure the vehicle maintains sufficient chassis clearance above obstacles.

At the lowest level, cascaded proportional-integral-derivative loops operate within the motor controller to provide joint-level control. These loops operate at 5 kHz, but only receive setpoint updates from the FSW control loops at 10 Hz.

The vehicle downlinks telemetry continuously, but also has the capability to store data on board. This feature is capable of storing all mobility relevant telemetry for discrete periods of

time long enough to cover critical operations and loss of signal. Telemetry is sent down at a nominal rate of 1 Hz but can be configured up to 10 Hz if desired and bandwidth is available. These data sets are outlined in Table 1.

3. Soil Mechanics and Terramechanics Basis

The mechanical properties and behavior of the lunar regolith have important implications on lander and mobility system design and performance (H. J. Hovland & J. K. Mitchell 1973; N. C. Costes et al. 1972; W. D. Carrier et al. 1991; V. T. Bickel et al. 2019). The surface regolith’s mechanical behavior and its interaction with hardware (e.g., rover wheels) are highly coupled with the regolith’s vertical and horizontal stress–strain properties (bearing and shear strength), which combine frictional and cohesive forces acting in the regolith. Typically, geotechnical properties are determined through a suite of standard laboratory tests or are derived from semiempirically developed stress–strain relationships used to predict vehicle mobility performance. The goal here is to derive regolith geotechnical properties from known mobility performance targeting bearing capacity, modulus of subgrade reaction, and shear strength via Bekker parameters. Although it has some shortcomings, the Bekker model has the most heritage with respect to modeling and predicting vehicle performance and is therefore the model of choice for this analysis. Historically, terrain (regolith) properties such as shear strength, cohesion, and angle of internal friction have been characterized in various ways with respect to wheel–soil interactions and mobility applications (U.S. Army Corps of Engineers 1948; M. G. Bekker 1962; B. M. D. Wills 1966; M. G. Bekker 1969; J. Y. Wong 1989; J. E. Bowles 1992; S. Shoop 1993; J. P. Bardet 1997; J. Y. Wong 2006). For the purpose of this manuscript, we specifically focus on using the estimated values of wheel slip, measured values of wheel normal load, and measured values of wheel sinkage from captured images to make further geotechnical deductions using theoretical relationships. To our knowledge, this method to determine the soil parameters from direct in situ vehicle measurements has not been performed, and the actual methodology may differ from what is described here. There is much to learn about the implementation of these semiempirical equations in this application, and other methods exist to extract terrain parameters from vehicle performance (L. Ding et al. 2015). Not only will the geotechnical properties be of value, but the lessons learned will directly impact the way in which rovers collect ground-truth data in the future.

3.1. Rover Wheel Slip

Physically speaking, wheel slip is the measurement of shear displacement in a granular media (i.e., soil or lunar regolith in our case) beneath a wheel. However, it is typically used in the

Table 1
VIPER Data Sources for Terramechanics and Geomechanical Investigations

Data Source	Key Parameters		Sampling Frequency	Resolution
Actuator Motor Controllers	The Motor Controllers report applied motor winding voltages between 0 and 36 VDC to the Rover FSW.		10 Hz	0.015 VDC
Wheel Module	<i>Actuator Currents</i>	Drive, steering, and suspension actuator currents are reported via the Motor Controller to the Rover FSW.	10 Hz	0.01 Amps-RMS
	<i>Actuator Velocities</i>	Drive, steering, and suspension actuator velocities are reported via the Motor Controller to the Rover FSW.	10 Hz	0.0015 rad s ⁻¹
	<i>Actuator Positions</i>	Steering and suspension actuator positions are reported via the Motor Controller to the Rover FSW.	10 Hz	0.0015 rad
	<i>Actuator Temperatures</i>	Motor winding and gearbox temperatures are captured and reported by the flight computer. Temperatures are required for accurate torque estimation at the joint output.	0.5 Hz	1.24°C
	<i>Suspension Torque Transducer</i>	The torque transducer and related Motor Controller circuitry measures suspension output torques between +/-297 N m.	10 Hz	0.07 N m
IMU (LN200S)	The IMU reports chassis linear accelerations (3-axis accelerometer) and chassis angular rates (3-axis gyroscope). Data stream is too high bandwidth for continuous downlinking but can be stored on board for select periods of time and downloaded as a file.		100 Hz	IMU acceleration resolution is a known and controlled access value.
IMUF Onboard Application	The IMU Filter (IMUF) onboard application aggregates the raw IMU data and downlinks the averaged chassis linear accelerations and angular rates.		10 Hz	N/A
Star Tracker	The star tracker (ST-16) returns the attitude of the chassis in the J2000 coordinate frame. The data only meets the required accuracy when the rover is stationary. The onboard star tracker I/O application processes the reported J2000 attitude into an estimation of the rover's attitude in the local mission frame using the onboard clock and ephemeris tables.		0.5 Hz for both the J2000 frame and local mission frame	N/A
Onboard Pose Estimator (PEST)	PEST provides the rover and the ground station with an estimated position (x, y, z) and attitude (quaternion [w, i, j, k]) of the rover during the mission, along with their corresponding covariance matrix values. For ease of processing, the reported attitude quaternion is also converted into Euler angles (roll, pitch, yaw).		10 Hz	N/A
Slip Estimator	The onboard slip estimator relies purely on internal sensing (joint encoders, IMU, and motor current sensors) to determine when to flag a potential embedding event. It also reports the onboard estimated amount of rover longitudinal slip (between 0 and 1).		10 Hz	N/A
Active Control	The inputs and outputs of the onboard active controls are downlinked. This data reports the current estimated ground clearance, each wheel's suspension linear offsets relative to the ideal wheel plane, and the attitude tracking controller error.		10 Hz	N/A
NavCams	The NavCams are a calibrated stereo pair that provide the primary imaging for rover navigation. The images can be binned on board to decrease the bandwidth utilization. This stereo pair is mounted on the mast with pan and tilt capability.		Variable	Field of view is 70° x horizontal and 70° vertical with an image resolution of 2048 × 2048 pixels.
AftCams	The AftCams are a calibrated stereo pair that provide secondary imaging for rover navigation. The images can be binned on board to decrease the bandwidth utilization. This stereo pair is mounted at the aft of the rover.		Variable	Field of view is 110° horizontal and 110° vertical with an image resolution of 2048 × 2048 pixels.

Table 1
(Continued)

Data Source	Key Parameters	Sampling Frequency	Resolution
HazCams	The HazCams are a set of four cameras, providing situational awareness around each wheel. The images can be binned on board to decrease the bandwidth utilization.	Variable	Field of view is 110° horizontal and 110° vertical 2048 × 2048 pixels
NIRVSS AIM	The AIM is an imaging system with eight LED colors integrated into the NIRVSS instrument. The images can be binned on board to decrease bandwidth utilization. The AIM field of view is positioned to look beneath the rover at the location of the drill foot.	Variable	Field of view is 35.7° horizontal and 35.7° vertical 2048 × 2048 pixels

field of terramechanics as a quantifiable metric to assess the rover wheel's interaction with the ground. Coupled with other details, it can be used to infer information such as driving efficiency, maximum slope climbing potential, and the likelihood of vehicle entrapment (i.e., getting stuck). Most importantly, it is an easily quantifiable metric that is commonly used in testing and simulation when assessing rover performance; thus, extensive wheel slip data exists on VIPER engineering units from Earth-based testing and simulations. Occasionally the term "Travel Reduction" is used more broadly when assessing full vehicle performance versus the individual wheel, but here the term "wheel slip" is used for both. Mathematically it is calculated as follows:

$$i = \frac{r_r \omega - v}{r_r \omega} \quad (3a)$$

where i is the calculated wheel slip ratio (unitless), r_r is the effective wheel radius (cm), ω is the rotational speed of the wheel (rad s^{-1}), and v is the linear speed of the vehicle or simply the linear speed of the wheel center with respect to the contacting terrain (cm s^{-1}). When driving, a torque is applied to the wheel and the wheel rotates, but without the same forward progress. Thus, the wheel rotates faster than the equivalent translation and a positive slip value result. Note that 100% slip occurs when the wheel is rotating with no forward progression. Negative slip occurs when the wheel is rotating more slowly than the equivalent translation (i.e., wheel skid as in down a hill).

Continuously monitoring wheel slip offers critical insight into drive progress, as well as understanding terrain properties and its changes as a function of geologic context and slope. Particularly, observing the changes in wheel slip, depending on the volatile existence, can strongly constrain the correlations of such changes with the presence of regolith-cementing volatiles in the shallow subsurface of the lunar south pole.

Important ancillary parameters include wheel rotation rate, direction, and orientation, as well as rover speed from wheel odometry. These values can be compared with actual distance traveled as measured from visual odometry. Routine images of the rover tracks to measure grouser imprint spacing—as performed by the Yutu-2 rover (L. Ding et al. 2022) and the Curiosity rover (A. Rankin et al. 2021)—from HazCam or rearward-looking NavCam/AftCam images will be useful to reconstruct wheel slip, as often as every 5 m or as frequently as possible.

3.2. Laboratory Testing of VIPER Slip Performance

Laboratory testing was conducted at the NASA Simulated Lunar Operations (SLOPE) Laboratory to verify the ability of VIPER to climb certain slopes on the Moon. The large simulant testbed in the SLOPE Lab consists of three primary sections: the flat "lane" ($12 \text{ m} \times 3 \text{ m} \times 0.3 \text{ m}$), the "tilt bed," which enables sloped terrain with hydraulic lifts ($6 \text{ m} \times 5 \text{ m} \times 0.3 \text{ m}$), and the "sink tank" ($12 \text{ m} \times 3 \text{ m} \times 0.6 \text{ m}$). This testing for VIPER utilized the tilt bed to simulate different slope angles and is filled with GRC-1, which is a lunar simulant developed to match the bulk mechanical properties of the lunar terrain observed during the various Apollo surface missions at the lunar equator (H. A. Oravec et al. 2010). An Optitrack motion tracking camera system is installed in the lab (A. Schepelmann & S. Gerdts 2022) to collect motion data that was used to determine vehicle slip. Tests were conducted utilizing VIPER's Moon Gravity

Representation Unit, or MGRU, which consists only of the mobility system, chassis, and IMU. MGRU's weight is roughly equivalent to VIPER's lunar weight in order to provide analogous traverse load conditions. These tests were conducted in a characterized loose GRC-1 with a relative density of approximately 15%–20% (C. Creager et al. 2017). Since regolith from the south pole of the Moon has not yet been sampled, this simulant was chosen because it is highly characterized (i.e., its mechanical properties are well understood), and in a loosened state, it is considered to be a challenging material to traverse, thus providing a helpful endmember constraint on VIPER performance. However, there are still questions related to the validity of this simulant and testing approach, especially with regards to the effect of gravity, for predicting operational performance at the lunar south pole. As explored in G. Butt (2024), it was determined that the gravitational scaling laws method demonstrated better correlation to single-wheel mobility test results collected during a reduced gravity parabolic flight, as compared to the method of testing a reduced mass vehicle in GRC-1 in a laboratory. This discrepancy between approaches for estimating vehicle performance on the Moon is outside the scope of this paper but stresses the need for ground-truth data.

Each test in the SLOPE Lab consisted of the rover driving directly uphill on a set incline, pausing, then driving backwards downhill through its own tracks. For each traverse, both uphill and downhill, the mean wheel slip was calculated based on the mean rotational speeds of the wheels and the linear speed of the vehicle (making the assumption that all wheels were traveling at the same speed). The slope angle versus mean wheel slip results from driving uphill are shown in Figure 9(a), and the results from driving downhill are shown in Figure 9(b). In a physical sense, at 0% wheel slip, the wheel is traveling at the commanded speed based on wheel rotational rate and an assumed rolling radius; at 100% slip, the wheel is rotating, but the linear speed is zero.

The laboratory testing conducted on the MGRU vehicle focuses on engineering development and requirement verification of the mobility system. Existing laboratory data sets for the MGRU vehicle do not contain high-fidelity sinkage measurements, as sinkage is not tied to mission requirements, nor was it easily quantifiable in this lab setup. However, sinkage could be estimated via images from the tests, similar to how it would be estimated during the mission. These images exist, but forward work is needed to estimate the sinkage.

3.3. Slip Estimation Techniques Employed in the VIPER Mission

During the VIPER mission, slip estimation is a critical metric for ensuring the rover's operational safety and navigational accuracy. VIPER utilizes two primary methods for estimating slip, each tailored to optimize the rover's performance across the challenging lunar terrain. These methods include onboard proprioceptive slip estimation and visual odometry-based slip estimation.

3.3.1. Onboard Proprioceptive Slip Estimation

The first method involves an onboard slip estimation system integrated into the FSW, which leverages proprioceptive sensors. This system is designed to continuously monitor and measure slip at 10 Hz using a sophisticated algorithm that compares real-time sensor inputs with a model verified using

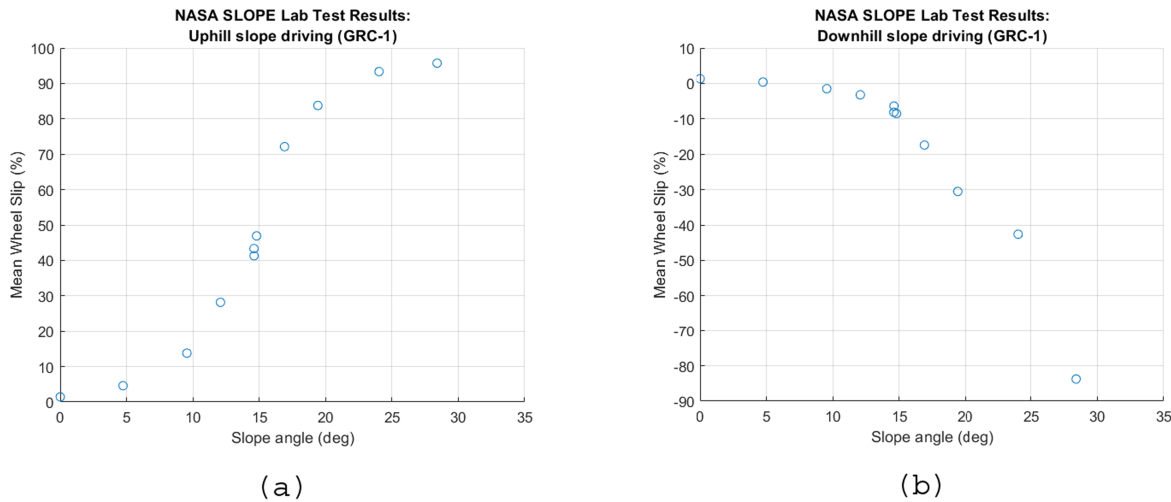


Figure 9. Laboratory test results collected on the VIPER MGRU test platform in the NASA SLOPE Lab. (a) Vehicle was driven uphill in loose GRC-1; (b) Vehicle was driven backwards downhill through tracks.

the MGRU test data and tuned using lunar terramechanics simulations. The MGRU data verification test includes streaming sensor data into the slip estimator software and comparing the estimated output with the ground-truth slip calculated using an OptiTrack motion capture system. The overall accuracy of the slip estimator is 93% evaluated over 99 tests of 5–10 m travel distances in varying terrain conditions (mixed, flat, sloped, GRC-1, or Fillite simulant; here, Fillite is a high sinkage simulant).

Simulations were conducted using Project Chrono and validated against MGRU test data across different soil simulants (GRC-1, Fillite, and granite fines). Both the simulation framework and the underlying software models were validated to ensure accurate response. Validation was performed by comparing slip estimates from the simulation with ground-truth slip measurements obtained from real-world experiments in laboratories. Although the model is designed to be gravity-independent in theory, we anticipate some residual gravity-related effects. To account for this, the slip estimation algorithm includes provisions for in situ tuning on the lunar surface using real-time data.

Key outputs such as wheel odometry, motor currents, and orientation estimates based on the IMU and the star tracker are analyzed to detect any anomalies indicative of slip, including both longitudinal and yaw-induced movements. The primary goal of this system is to prevent the rover from encountering hazardous excessive slip scenarios, thus safeguarding its operational integrity. The output slip estimations can be compared against other slip estimates generated by additional lower-frequency visual odometry.

3.3.2. Visual Odometry-based Slip Estimation

The second method employs visual odometry to ascertain the average slip over a designated straight-line trajectory, typically ranging from 2–8 m. This technique utilizes stereo image pairs from the NavCams captured at the commencement and conclusion of each drive segment. Through the application of the Iterative Closest Point algorithm, the system calculates the actual distance traversed by the rover (P. J. Besl & N. D. McKay 1992). The results from the visual odometry are then juxtaposed with the data from the onboard wheel odometry, serving as a ground-truth benchmark to refine slip

estimations further. The accuracy of this visual odometry-based estimation has been rigorously validated through simulation, demonstrating a precision level of ± 0.2 m with a 95% confidence interval. Consequently, this translates to an anticipated error in slip estimation ranging between 2.5% and 10%, depending on the length of the drive segment.

3.3.3. AIM Camera Velocity Estimation

The Ames Imaging Module (AIM) camera is part of VIPER's NIRVSS instrument and provides narrow grayscale images captured at a rate of 0.5 Hz (Table 1). Given the rover's anticipated forward velocity during driving, overlap will exist between subsequent images captured by AIM. Using this overlap, velocity between frames can be estimated using computer vision approaches like optical flow analysis (K. Nagatani et al. 2000; J. Campbell et al. 2004; P. Muller & A. Savakis 2017). This technique allows for the calculation of motion vectors between corresponding pixels in the overlapping regions, providing valuable information about the rover's in situ forward velocity. This data source also provides a redundant measurement to the velocity vector generated by VIPER's IMU. When combined with commanded forward velocity measurements calculated using each wheel's effective radius and angular velocity as measured by drive actuator resolvers, this information enables wheel slip to be calculated while the rover is driving on the lunar surface.

3.4. Terrain Slope Estimation Techniques Employed in the VIPER Mission

VIPER's integrated mobility system is equipped with four independently actuated suspensions, as previously described. This system facilitates adjustable chassis ground clearance (7–42 cm), pitch ($+/-20^\circ$), and roll ($+/-15^\circ$) essential for maintaining stability and operability on uneven lunar surfaces. The suspension kinematics is used to determine a best-fit plane, which represents the local terrain slope beneath the rover in relation to the vehicle's chassis frame.

To estimate the slope in a lunar surface frame, the rover utilizes a fusion of data from its IMU and star tracker. These components continuously calculate the rover's orientation in terms of roll, pitch, and yaw. This fusion results in a robust

pose estimation, which, when combined with the suspension position-based slope estimation, yields an average slope of the terrain directly under the rover's footprint in the lunar frame. This slope is referred to as the kinematic slope.

However, it is crucial to acknowledge the limitations of this kinematic-based slope estimation. The methodology assumes a relatively uniform terrain, primarily relying on the suspension geometry and the rover's pose. It does not account for uneven wheel sinkage, undulations, rocks, craters, and other forms of terrain irregularities that are characteristic of lunar landscapes. These elements can introduce significant errors in the slope estimation, leading to discrepancies between the estimated and actual terrain conditions.

For more precise terrain information, the rover employs its stereo camera system to generate detailed 3D maps of the surrounding terrain. However, the dynamic nature of the rover's movement, including wheel slip and the time delay in processing camera data, means that the terrain maps and the rover's pose are not always synchronized positionally. As a result, the actual terrain slope directly underneath the rover, as calculated by the stereo system, may not align perfectly with the mapped data at any given moment.

3.5. Rover Sinkage

Wheel sinkage is defined as the deformation of the supporting surface from its original, undisturbed surface, measured normal to the direction of travel (R. He et al. 2020). This metric is not as easily measurable as wheel slip but is still valuable when assessing rover performance. For vehicles of similar mass, size, and wheel geometry, higher sinkage implies “weaker” soil or excessive slip, which allows for some interpretation of traversed terrain conditions because the response is then decoupled from the vehicle and tire geometry.

Sinkage of the wheels into the surface can help bound the bearing (shear) strength and near-surface porosity of the regolith. Here, it is important to note that shear stress developed in the soil may also lead to additional sinkage, termed “slip-sinkage.” In certain types of soil, generally loose frictional media, slip-sinkage may be significant and should be accounted for especially when evaluating bearing capacity. Slip-sinkage is due to longitudinal motion of the soil under the wheel during driving as well as lateral motion imposed by the grousers and can potentially be controlled under 40% wheel slip (L. Ding et al. 2010). In addition, the mobility design requirements of the VIPER mission defined a maximum of 40% slip up a maximum slope of 15°, bringing the impact of slip-sinkage for this mission into question.

Changes in wheel sinkage during driving, taking other factors like terrain slope and current wheel slip into account, could also help in detecting the presence of near-surface regolith-cementing volatiles, e.g., if sinkage drastically changes while other terrain parameters remain constant. Such behavior would be a clue possibly indicating more complex structure in the regolith, i.e., present volatiles cementing grains together, but it would not itself be a singular determining factor. Additional information from other onboard instruments like NIRVSS and NSS would be needed to make this determination. This measurement is best done from images of the wheel tracks either by stereo AftCam or “chin-down” NavCam images, or from mono HazCam images. The desired cadence of these observations is as frequently as possible, up to every 5 m.

3.5.1. Image Processing Sinkage Estimation

VIPER's HazCams provide a 110° × 110° field of view of each rover wheel and are the only camera source guaranteed to have the rover's wheels in their field of view at all times. By leveraging the known locations, intrinsic and extrinsic camera parameters, the vehicle's body pose, and wheel linkage kinematics, imaging data can be used to estimate wheel sinkage. In this approach, rover kinematics can be used to calculate the pose of wheels, which, when combined with visual information extracted from calibrated camera images, can be used to measure the amount of sinkage experienced by each rover wheel. To extract detailed information about the position of each wheel relative to the lunar surface, computer-aided design geometry of the rover wheel could then be overlaid with these calibrated images and combined with kinematics information to enable the collection of high-accuracy sinkage data from each camera image.

As seen in Figure 4, the inboard face of the Wheel contains a geometric quadrature pattern with known geometry. The quadrature pattern's inner ring, rivet heads, sheet metal tab features, and inner rim edge all provide fiducials of varying yet known dimensions. These individual features can be combined as independent measurements from a single image to improve the sinkage estimate. It is understood that the empty portion of the quadrature pattern provides less information if it is the portion of wheel engaged with the regolith.

Additionally, both the rover's AftCam and NavCam systems can be used to capture images of wheel tracks left behind as VIPER's wheels displace regolith on the lunar surface, enabling secondary inferences about both wheel sinkage and gross amount of wheel slip over distances within an image. Image processing for wheel sinkage is also dependent on the lighting conditions and sunlight direction with respect to the vehicle, as these conditions affect the integrity of the image captured.

3.6. Bearing Capacity Analysis through Classical Geotechnical Methods

Traditional geotechnical models for bearing capacity and subgrade reaction can be used to back out mechanical descriptors of the regolith. In previous efforts to assess soil properties, wheel sinkage is usually described using either the concept of subgrade reaction or bearing capacity (A. L. Filice 1967; J. Eggleston et al. 1968; H. J. Moore 1970; W. D. Carrier et al. 1991; V. Bickel & D. Kring 2020). The modulus of subgrade reaction, k , is usually derived assuming a purely elastic response of the regolith using a Winkler model (E. Winkler 1867) and can be noted as:

$$q = kd \quad (1)$$

with q as the applied load (bearing pressure) and d as the depth (W. D. Carrier et al. 1991). It should be noted that Equation (1) does not account for sinkage due to shear displacement of the soil (typically referred to as “slip-sinkage”). For low wheel slip cases, slip-sinkage can be considered negligible. With (statistically) known values for k and q , the sinkage of a wheel can be estimated when wheel slip is estimated to be near 0% such as driving down on flat terrain or a shallow incline. The concept of bearing capacity for a circular footing assumes a plastic deformation of the regolith and can be noted as

(K. Terzaghi 1951):

$$q = 1.3cN_c + q_0N_q + 0.3\gamma BN_\gamma \quad (2)$$

where c is the cohesion, $q_0 = \gamma D$ is the overburden pressure where D is the footing depth and γ is the regolith's unit weight, B is the diameter of a rectangular footing, and N_c , N_q , and N_γ are the bearing capacity factors derived from the regolith's angle of internal friction (D. P. Coduto et al. 2011). As for the modulus of subgrade reaction, bearing capacity equations can be used to estimate wheel sinkage as long as the applied load (bearing pressure) is known, and the wheel slip is again estimated to be near 0%.

It is important to note that contrary to immediate沉降 that occurs as a direct response to an applied load, as described by the modulus of subgrade reaction and bearing capacity, regolith consolidation describes the continuous (creeping) mechanical deformation of the regolith in response to a load that is continuously applied over extended periods of time (D. P. Coduto et al. 2011). Consolidation, a long-term effect on the order of days or more, does not directly affect exploration activities like roving, which are short-term, on the order of seconds, though it will affect permanent infrastructure placed on the lunar surface.

3.7. Bearing and Shear Analysis through Bekker Methods

The typical civil engineering soil mechanics formulas for bearing capacity, discussed in Section 3.6, have been generalized and modified over the years for application to vehicle mobility—resulting in semiempirical methods for determining vehicle performance. However, for a wheel driving in granular soil, shear failure is often the driving failure mode; thus, equations are needed to account for the effects of shear displacement and shear stress under a wheel as well. The most widely accepted semiempirical methods for quantifying the interaction between homogeneous soft terrain and a quasi-static rigid wheel is the bevameter method used to determine bearing strength and shear strength through vertical and horizontal stress-strain relationships defined by M.G. Bekker and J.Y. Wong (M. G. Bekker 1956; M. G. Bekker 1960; M. G. Bekker 1969; J. Y. Wong 1980; J. Y. Wong 1989; J. Y. Wong 2006) and Z. Janosi & B. Hanamoto (1961), respectively (Equations (3) and (4)). See J. Y. Wong (1989) for a step-by-step approach to analyze plate-sinkage and shear-bevameter data.

$$p = \left(\frac{k_c}{b} + k_\varphi \right) z^n \quad (3)$$

$$\tau = (c + \sigma \tan \varphi)(1 - e^{-j/K}) \quad (4)$$

In Equation (3), p is the pressure under the wheel footprint, b is the smaller dimension of the rectangular loading area or the radius of a circular plate, z is the soil depth or sinkage, n is the empirical soil value that defines the shape of the penetration curve, and k_c and k_φ are the moduli of deformation with respect to soil cohesion and friction angle. In Equation (4), τ is the estimated shear stress in the soil calculated from the applied wheel torque and diameter, c is the soil cohesion, σ is the wheel contact pressure, φ is the soil friction angle, j is the shear displacement estimated using linear wheel rotation distance and vehicle speed, and K is the shear deformation modulus of the soil. Note that $\tau_{\max} = c + \sigma \tan \phi$, which is

simply Coulomb's equation for shear strength or maximum shear stress. Equation (4) can therefore be simplified to Equation (5).

$$\tau = \tau_{\max} (1 - e^{-j/K}) \quad (5)$$

It is important to note that the basis for Equations (3) and (4) assume a smooth, rigid, cylindrical wheel or track. However, recent studies (K. Skonieczny et al. 2012) have indicated that grousers can have a significant impact on how the tire interacts with granular soil. Thus, the direct application of the described methodology for determining sinkage and shear stress with the VIPER mobility system may be complicated by the use of relatively tall grousers on the wheels with respect to the overall diameter (L. Ding et al. 2010), though these empirical relationships provide us with a starting point for comparison. While the bevameter technique, with appropriately sized plates and representative annular rings, may be used to predict (with relative confidence) the mean values of wheel sinkage and shear forces, the dynamic effects or oscillations in force due to grousers are not accounted for by these models (R. A. Irani et al. 2011). Terrain interaction models that estimate the effect of or explicitly consider grousers and their effects (K. Legnemma et al. 2004; G. Ishigami et al. 2007, 2009; R. A. Irani et al. 2011; Z. Jia et al. 2012; R. He et al. 2019) can instead be applied, though their development is much less mature. For the sake of these efforts, assuming a constant soil displacement rate beneath the wheel may be sufficient.

In principle, the objective is to estimate soil bearing and shear strength with the use of estimated Bekker parameters in Equation (3), n and k' (where $k' = (\frac{k_c}{b} + k_\varphi)$), by using the known normal force on each wheel and wheel geometry to estimate p and measurements of the sinkage, z . Note that k' is similar to k from Equation (1), but here it is dependent on the plate size. Since, the wheels are all the same size, the value of b is assumed to be the same, which does not provide for an opportunity to estimate the independent values of k_c and k_φ . Ideally, the low incline terrain mission data can be plotted in terms of pressure versus sinkage, and a least-squares fit to the Bekker equation can be applied to determine n and k .

Similarly, using the known normal force on each wheel and wheel geometry to estimate σ , measurements of wheel torque and known radius to calculate the shear stress τ , and finally encoder data and wheel track images to estimate shear displacement j , Equation (4) can be used to infer K , c , and ϕ . Following the J. Y. Wong (1989) methodology, an optimum value of K is calculated using the following equation:

$$K = - \frac{\sum (1 - \tau/\tau_{\max})^2 j^2}{\sum (1 - \tau/\tau_{\max})^2 j [\ln(1 - \tau/\tau_{\max})]} \quad (6)$$

Then, an average K -value from a minimum of three to five different contact pressures is calculated. Here we can use the normal pressure values from each of the wheels to determine the mean K -value. This K -value is then used in Equation (5) to determine the optimum value of the maximum shear stress τ_{\max} , as it is not necessarily the maximum value observed during test (J. Y. Wong 1989). An iterative procedure is followed, where τ_{\max} is first selected as the maximum value of τ resulting from the test. Wong's goodness-of-fit equation is solved, and a new value of τ_{\max} is iteratively selected until the goodness-of-fit value is minimized (see J. Y. Wong 1989 for full details on the analysis). Finally, using σ and τ_{\max} , the

cohesion and friction angle of the soil can be estimated using the Mohr-Coulomb failure criterion and implementing a least-squares approach.

It should be noted that in order to estimate the shear strength of the regolith, τ_{\max} , there must be driving conditions that produce high slip in order for the shear stress, τ , to reach a high enough level. For VIPER, this may only occur when driving on slopes. Further work is needed to determine how to derive the necessary parameters while on an incline versus on a flat surface.

4. Mission Operations

The mobility system is utilized in the majority of VIPER active surface operations, disengaged only for drilling. In the VIPER mission operations design, there are three primary operation modes: “rails,” “prospecting,” and “drilling.” Investigations of the geotechnical properties of the lunar surface via the instruments available through the mobility system can be conducted during both rails and prospecting driving modes. While the detailed traverse path is provided by E. Balaban et al. (2025, in preparation) and A. Colaprete et al. (2025b, in preparation, submitted this issue), the 2025 October landing plan targets a 5 km by 5 km area centered at 31.6218° E, 85.42088° S on Mons Mouton. The planned traverse path totals a traverse distance of ~ 37 km and contains 27 science stations with various ISRs, including four permanently shadowed regions (PSRs; E. Balaban et al. 2025, in preparation).

The mission design has a traverse that begins at lander egress and ends at end of mission. This traverse progresses to numerous “science stations,” which are large areas of interest that each nominally contain three drill locations (D. Lim et al. 2025, in preparation, submitted this issue; Z. Mirmalek et al. 2025, in preparation, submitted this issue). Although exact boundaries of any science station may be modified as new data is obtained by VIPER or other sources, the equivalent area, for planning, is roughly 3800 m^2 . Ice stability regions (ISRs) are at the center of VIPER’s traverse planning process, and the science stations are chosen to interrogate these ISRs. These regions are areas where it has been determined from orbital data that water ice could physically exist on or near the surface of the Moon (M. Siegler et al. 2015). The VIPER mission designates four ISR types based on the maps developed by M. Siegler et al. (2015) including “dry” where there is no evidence supporting ice stability in the top 85 cm of regolith; “deep” where there is evidence of ice stability within the regolith at depths of 20–85 cm; and “shallow” where evidence supports ice stability at depths of 0–20 cm in the regolith. The fourth ISR type is “surficial” where surface temperatures are sufficient for water ice to be stable at the surface (most of these are PSRs). A science station is defined as being dominated (at least 66% by area) of a particular ISR type. Within any science station, to meet the geostatistical mapping needs, the linear coverage by the rover within a science station should be $> 10\%$ (15% goal). As the rover drives, it sweeps out an approximate 2 m wide area of measurement, which in turn leads to a total drive distance required of 190 m (285 m goal) per station. Adjacent station locations have additional requirements to be separated by at least 100 m (A. Colaprete et al. 2025b, in preparation). VIPER’s surface mission traverse design is optimized for lunar regions that receive prolonged periods of sunlight (short lunar nights). As such, the mission duration will

be more than 100 Earth days, and result in a traverse distance of up to 20 km.

During both prospecting and rails, NSS, MSolo, the NIRVSS spectrometers, and NIRVSS Longwave Calibration Sensor are operating continuously. When operating continuously, MSolo and the NIRVSS spectrometers have the ability to change the specifics of their modes such as amu precision, spectral binning, and data rates, as requested by the VIPER science team. In addition to taking lower-resolution single-color NIRVSS AIM images at 0.5 Hz during driving, when the rover is prospecting in a science station, the NIRVSS AIM can be configured to take higher-resolution multicolor images when the rover is temporarily stopped during waypoints for panoramas and stereo images by the rover cameras. TRIDENT is off and stowed during any driving operation.

Rails driving has the primary objective of progressing from one science station to the next, which necessitates propulsion at the maximum rover commanded speed of 20 cm s^{-1} . The rover drivers select commanded waypoints to avoid obstacles during rails driving. Some of the science payloads may be operated in a more limited data collection capacity during rails driving.

Prospecting driving occurs within a science station and is focused on maximizing the surface analysis possible while progressing to drill site locations. This means that the prospecting drive path is not specifically the fastest route to the drill location at any given time, and the rover is driven at a maximum speed of 10 cm s^{-1} . Rover camera (Nav/Aft/HazCam) image capturing occurs only at waypoints during both driving modes. The NIRVSS instrument has an additional function of taking images at each waypoint during prospecting driving. A traverse path at each science station may be planned before the rover arrives on the Moon by accounting for science investigations. Within the traverse path, the first and second drill locations, known as Drills A and B, will be fixed, while the third drill location, or Drill C, will be kept flexible to be replanned during real-time operations. This operational approach allows the VIPER Science Team to give scientific input, including that for the geotechnical properties, to the traverse planning. Therefore, a planned traverse path can account for detailing the geotechnical properties based on the rover’s mobility performance. Once a targeted drill site is reached within the science station, the rover enters drilling mode, which re-configures the system and locks out rover mobility in preparation for drilling. The rover progresses “on rails” between science stations and then, upon entering the science station, is switched to prospecting.

Since rails and prospecting modes are both driving operations, it is then possible to extract data from the various sources within the mobility system during these periods in addition to the science instrumentation data. A combination of the mobility system data and science instrument data is to be used to make assessments of rover slip and sinkage both during rails and prospecting driving as well as during prescribed experimental operations, as described next.

5. Anticipated Scientific Investigations

Analyses of VIPER’s mobility data produced from the active control scheme in concert with terrain characterizations from the scientific instruments can be made throughout the mission profile. The data made available through the mobility system and necessary controls provide critical insight

Table 2
Experiment #1 Anticipated Data Products

Data Product	Description
Wheel slip versus slope angle plot	Average slip and slope values measured during “constant-slope” regions of each drive segment
Wheel sinkage versus slope angle plot	Average sinkage and slope values measured during “constant-slope” regions of each drive segment
Wheel normal load versus wheel slip plot	Average wheel normal load and wheel slip values measured during “constant-slope” regions of each drive segment
Wheel normal load versus wheel sinkage plot	Average wheel normal load and wheel sinkage values measured during “constant-slope” regions of each drive segment
Estimation of lunar regolith bearing and shear strength	Bearing strength and shear strength values for the terrain driven during testing determined using VIPER rover data, laboratory test data, and terramechanics and geotechnical modeling; refer to Section 3.6. and 3.7.

into the lunar surface and how the rover as deployed responds. These insights are relevant to high-priority science goals identified in the Artemis III Science Definition Team Report (NASA 2020a) related to regolith processes and weathering, including “Investigation 1f-1: Determine physical properties of regolith at diverse locations of expected human activity.” To address the critical issue of estimating geotechnical properties at the surface of the lunar south pole, the VIPER mission lays out two specifically scoped experiments that will happen during discrete portions of the mission.

5.1. Experiment #1: Assessment of Vehicle Performance on Highlands Terrain during Rails Driving

The first of two specifically designed experiments to assess the geotechnical properties of the lunar south pole is centered on driving VIPER up slopes in dry ISRs (i.e., regions with no evidence supporting ice stability in the top 85 cm) during rails. The goal is to drive the rover uphill on multiple sloped surfaces with estimated slope angles ranging from 0° to 15°. Wheel slip and slope data from these driving segments will be used to produce a notional slope versus wheel slip curve for the lunar south pole highlands terrain, like those derived for the MGRU shown in Figure 9. Estimated wheel sinkage and measured wheel load will be used to deduce ground-truth quantities for regolith properties, including the modulus of subgrade reaction and bearing capacity at wheel slips estimated to be near 0%, refer to Section 3.6. on bearing capacity.

This experiment should be conducted on at least 10 sections of rails driving segments that are each at 10 m long, located at disparate locations within dry ISRs throughout the greater mission traverse. The rover will be driven directly uphill during these defined sections of rails driving, though obstacles (e.g., boulders, craters) should be avoided as needed. Within each driving segment, there should be multiple “constant-slope” regions (at least 2 m in length) where the slope variation is minimal (+/-2°); wheel slip and slope angle will be averaged for each constant-slope region. Slopes to be traversed need to have angles within the full 0°–15° range, which represents flat ground to the mission slope traversal requirement, respectively. The higher-priority slope values are 0° (+/-2) and between 7° and 15° (+/-2) to help bound the slip versus slope curve. The vehicle should be driven as straight as possible to avoid slip and sinkage contributions from steering, though these contributions are minimized with the use of steering actuators instead of a skid-steer design. If a steering maneuver is required, AftCam images can be captured to give context. If fresh crater ejecta is encountered, it should be avoided if possible, as it is expected that these areas will exhibit higher-than-nominal slip and sinkage due to the less consolidated regolith (N. C. Costes et al. 1972; W. D. Carrier

et al. 1991). For additional opportunities, driving uphill can occur during prospecting driving segments as long as the slope conditions and length meet the experiment requirements. Images from the wheel HazCams will be captured at each waypoint during each partial rails segment (approximately every 5 m) to assess wheel sinkage. AftCam images will be collected at each waypoint to collect visual context data of the wheel tracks to assess slip estimations. This experiment will yield numerous important data products (detailed in Table 2) to help assess the geotechnical properties of nominally dry, sloped highlands terrain, which will be compared to those derived for other locations on the Moon.

5.2. Experiment #2: Effect of Volatiles on Geotechnical Properties during Science Station Prospecting

The second investigation of interest is assessing whether or not there are perceptible mobility performance differences in a variety of soil property states, including (A) volatile-bearing versus volatile-free terrains, (B) younger versus older crater structures (ejecta and interiors), and (C) currently illuminated versus shaded areas. These investigations will enable the testing of multiple scientific hypotheses derived from our current state of knowledge of the lunar polar environment.

For example, (A): do volatile-bearing terrains have higher strength (resulting in less wheel sinkage) than volatile-free terrains? Experiments using lunar simulants suggest that material strength and penetration resistance increase with increasing water mass and density (L. Gertsch et al. 2006; C. Pitcher et al. 2016).

Additionally, (B): do younger crater structures have different geotechnical properties (such as variations in wheel sinkage and slip) than older crater structures? One remarkable geological variation in craters at different ages may be the existence of different porosity. Analyses of crater reflectance (K. E. Mandt et al. 2016), thermal inertia (J. L. Bandfield et al. 2014, 2017), topographic roughness (A. N. Deutsch et al. 2020; J. Wang et al. 2020), and block distributions (R. R. Ghent et al. 2014; Y. Li et al. 2018; C. M. Elder et al. 2019) suggest that fresh craters are associated with more porous ejecta and effective regolith strength may increase over time as materials are broken down and become more compacted. Related to the porosity variation, the boulder (particle) size-frequency distributions depend on the crater age and location. In addition to ejecta blankets, crater rims and slopes in general host larger particles than other regions (A. T. Basilevsky et al. 2013; C. I. Fassett et al. 2018; M. Pajola et al. 2018; R. N. Watkins et al. 2019). However, they are continuously degraded and redistributed by further micrometeoroid impacts (A. T. Basilevsky et al. 2013; A. T. Basilevsky et al. 2015; F. Hörz et al. 2020) or buried

Table 3
Experiment #2 Anticipated Data Products

Data Product	Description
Wheel slip versus slope angle plot	Average slip and slope values measured during “constant-slope” regions of each drive segment
Wheel sinkage versus slope angle plot	Average sinkage and slope values measured during “constant-slope” regions of each drive segment
Wheel normal load versus wheel slip plot	Average wheel normal load and wheel slip values measured during “constant-slope” regions of each drive segment
Wheel normal load versus wheel sinkage plot	Average wheel normal load and wheel sinkage values measured during “constant-slope” regions of each drive segment
Estimation of lunar regolith bearing and shear strength for terrain states tested	Bearing strength and shear strength values for the terrain driven during testing determined using VIPER rover data, laboratory test data, and terramechanics and geotechnical modeling. Terrain states to be evaluated separately to determine if differences are apparent.
Wheel slip and tested terrain state correlation	Tabulated average wheel slip values for a given terrain state
Wheel sinkage and tested terrain state correlation	Tabulated average wheel sinkage values for a given terrain state

by incoming ejecta from other craters and topographic diffusion (C. I. Fassett & B. J. Thomson 2014; D. A. Minton et al. 2019; C. I. Fassett et al. 2022; M. Hirabayashi et al. 2024). Therefore, older craters tend to have smaller particles spatially (C. I. Fassett et al. 2018; S. Vanga et al. 2022).

Finally, (C): does the regolith in shaded regions have higher porosity (causing more sinkage and slip) than regolith in illuminated regions? Laboratory experiments of thermal cycling (P. T. Metzger et al. 2018) and orbital measurements of regolith reflectance properties (G. R. Gladstone et al. 2012) and thermal inertia (P. O. Hayne et al. 2017) suggest that regolith inside PSRs may have relatively high porosity, potentially up to 70% inside PSRs versus 40% outside of PSRs (G. R. Gladstone et al. 2012).

In order to best understand the mobility response due to soil property states, the assessments should be conducted on as flat of terrain as possible while still meeting the desired soil property state constraint to avoid inducing slip and sinkage from sloped terrain. At each location, the rover should be driven one “partial prospecting segment” (at least 5 m) on relatively flat terrain (0° $+/- 2^\circ$). The objective of this investigation is to use wheel slip and sinkage to evaluate a range of potential soil conditions. Continuous knowledge of wheel slip is important for understanding regolith properties and their changes as a function of geologic context. Sinkage of the wheels into the surface can help infer the bearing strength, shear strength, and near-surface porosity of the regolith. Changes in wheel slip and sinkage could also be correlated with the presence of regolith-cementing volatiles in the near-surface/shallow subsurface.

The experiment should include driving the rover through a minimum of seven unique soil conditions encompassing ISR types (surface, shallow, deep, and dry), crater ejecta ages (young and old), and current regolith illumination conditions (sunlit and shadowed). Each defined condition should be tested at least twice, not driving over previously laid tracks. At waypoints, discrete images of wheels with the HazCams should be taken to observe wheel sinkage and with the AftCams to observe the driven wheel tracks. The rover needs to operate in its prospecting configuration during each partial prospecting segment to infer soil properties. Given this requirement, this experiment can be integrated into existing periods where prospecting mode is utilized with specific attention paid to target soil conditions to be driven over. This experiment will deliver important data products (Table 3) correlating bulk lunar regolith response to soil state parameters like volatiles content, temperature, and porosity.

6. Summary

The VIPER mission poses a unique opportunity to collect in situ terramechanics data throughout its operations on the lunar south pole, and this paper outlines methodology that can support the estimation of geotechnical parameters from that in situ data. A better understanding of the geotechnical characteristics of the lunar south pole provides important context for the lunar surface environment which VIPER—and all following robotic and crewed missions—are tasked with investigating. VIPER can use a combination of its mobility system and a capable suite of instrumentation to collect the complimentary in situ measurements required to make deductions about the geotechnical characteristics of the lunar surface. This approach is able to deliver multiple, separate estimates of wheel slip and sinkage, enabling the cross-comparison of the individual measurements. Data collected from VIPER can also be compared to the data collected from the Yutu-2 rover (L. Ding et al. 2022) by similar means. Specific experiments are laid out to investigate the vehicle’s response (e.g., wheel slip and sinkage) on nominally dry, sloped regolith as well as on nominally flat regolith that is orbitally estimated to be thermally stable for volatiles. These experiments represent targeted portions of the mission dedicated to making geotechnical assessments. However, it is possible to collect slip and sinkage data throughout the mission profile to make broader assessments of geotechnical characteristics of the lunar south pole and the vehicle’s mobility performance. This work showcases how VIPER can address the imperative need to understand the bulk geotechnical properties of the lunar south pole, which in turn helps to maximize the safety and science return of the Artemis campaign.

Acknowledgments

This work was supported by the NASA Science Mission Directorate (SMD) and the NASA Space Technology Mission Directorate (STMD). We acknowledge support from NASA’s Planetary Science Division Lunar Discovery and Exploration Program (PSD/LDEP) in SMD. VIPER was made possible by the work of the Resource Prospector team, which was supported by the NASA Advanced Exploration Systems Program. ProtoInnovations supported work described under Section 2.1 Active Control Scheme, Section 3.2 Laboratory Testing of VIPER Slip Performance, and Section 3.3.1 Onboard Proprioceptive Slip Estimation, under an SBIR Phase III contract No. 80NSSC22CA176.

ORCID iDs

- Erin Rezich  <https://orcid.org/0009-0009-4015-0656>
 Valentin T. Bickel  <https://orcid.org/0000-0002-7914-2516>
 Alexander Schepelmann  <https://orcid.org/0000-0001-9014-2173>
 Kimberly Ennico-Smith  <https://orcid.org/0000-0002-8847-8492>
 Ariel Deutsch  <https://orcid.org/0000-0001-9831-3619>
 Masatoshi Hirabayashi  <https://orcid.org/0000-0002-1821-5689>

References

- Arvidson, R. E., Anderson, R. C., Haldemann, et al. 2003, Physical Properties and Localization Investigations Associated With the 2003 Mars Exploration Rovers, *JGRE*, **108**, 8070
 Bandfield, J. L., Song, E., Hayne, P. O., et al. 2014, Lunar Cold Spots: Granular Flow Features and Extensive Insulating Materials Surrounding Young Craters, *Icar*, **231**, 221
 Bandfield, J. L., Cahill, J. T. S., Carter, L. M., et al. 2017, Distal Ejecta from Lunar Impacts: Extensive Regions of Rocky Deposits, *Icar*, **283**, 282
 Basilevsky, A. T., Head, J. W., & Horz, F. 2013, Survival Times of Meter-sized Boulders on the Surface of the Moon, *P&SS*, **89**, 118
 Basilevsky, A. T., Head, J. W., Horz, F., & Ramsley, K. 2015, Survival Times of Meter-sized Rock Boulders on the Surface of Airless Bodies, *P&SS*, **117**, 312
 Bardet, J. P. 1997, Experimental Soil Mechanics (Upper Saddle River, NJ: Prentice-Hall)
 Bekker, M. G. 1956, Theory of Land Locomotion (Ann Arbor, MI: Univ. Michigan Press)
 Bekker, M. G. 1960, Off-the-Road Locomotion (Ann Arbor, MI: Univ. Michigan Press)
 Bekker, M. G. 1962, Land Locomotion on the Surface of Planets, *ARSJ*, **32**, 1651
 Bekker, M. G. 1969, Introduction to Terrain-vehicle Systems (Ann Arbor, MI: Univ. Michigan Press)
 Besl, P. J., & McKay, N. D. 1992, A Method for Registration of 3D Shapes, *ITPAM*, **14**, 239
 Bickel, V., & Kring, D. 2020, Lunar South Pole Boulders and Boulder Tracks: Implications for Crew and Rover Traverses, *Icar*, **348**, 113850
 Bickel, V. T., Honniball, C. I., Martinez, S. N., Rogaski, A., Sargeant, H. M., et al. 2019, Analysis of Lunar Boulder Tracks: Implications for Traffability of Pyroclastic Deposits, *JGRE*, **124**, 1296
 Bowles, J. E. 1992, Engineering Properties of Soils and Their Measurement (New York: McGraw-Hill)
 Butt, G. 2024, Exploring Granular Scaling Laws via Parabolic Flight Experiments to Advance Lunar Rover Mobility Predictions, Master's thesis, Concordia Univ.
 Campbell, J., Sukthankar, R., & Nourbakhsh, I. 2004, Techniques for Evaluating Optical Flow for Visual Odometry in Extreme Terrain, in 2004 IEEE/RSJ Int. Conf. on Intelligent Robots and Systems (IROS), 4 (Piscataway, NJ: IEEE), 3704
 Carrier, W. D., Olhoeft, G., & Mendell, W. 1991, The Lunar Sourcebook (Cambridge: Cambridge Univ. Press),
 Coduto, D. P., Yeung, M.-C. R., & Kitch, W. A. 2011, Geotechnical Engineering: Principles and Practices (London: Pearson)
 Costes, N. C., Farmer, J. E., & George, E. B. 1972, NASA Tech. Rep. R-401, NASA, <https://sma.nasa.gov/SignificantIncidents/assets/apollo-15-mission-report.pdf>
 Creager, C., Asnani, V., Oravec, H., & Woodward, A. 2017, NASA/TP 2017-219384, NASA, <https://ntrs.nasa.gov/citations/20170010706>
 Deutsch, A. N., Head, J. W., Neumann, G. A., Kreslavsky, M. A., & Barker, M. K. 2020, Assessing the Roughness Properties of Circumpolar Lunar Craters: Implications for the Timing of Water-ice Delivery to the Moon, *GeoRL*, **47**, e2020GL087782
 Ding, L., Gao, H., Deng, Z., et al. 2010, Wheel Slip-sinkage and Its Prediction Model of Lunar Rover, *J. Cent. South Univ. Technol.*, **17**, 129
 Ding, L., Gao, H., Deng, Z., et al. 2011, Experimental Study and Analysis on Driving Wheels' Performance for Planetary Exploration Rovers Moving in Deformable Soil, *JTerr*, **48**, 27
 Ding, L., Gao, H., Liu, Z., et al. 2015, Identifying Mechanical Property Parameters of Planetary Soil Using In-situ Data Obtained from Exploration Rovers, *P&SS*, **119**, 121
 Ding, L., Zhou, R., Yuan, Y., et al. 2022, A 2-Year Locomotive Exploration and Scientific Investigation of the Lunar Farside by the Yutu-2 Rover, *Sci. Robot.*, **7**, 62
 Eggleston, J., Patterson, A., Throop, J., Arant, W., & Spooner, D. 1968, Lunar Rolling Stone, *PgE*, **34**, 246
 Elder, C. M., Douglass, B., Ghent, R. R., et al. 2019, The Subsurface Coherent Rock Content of the Moon as Revealed by Cold-Spot Craters, *JGRE*, **124**, 3373
 Fassett, C. I., Beyer, R. A., Deutsch, A. N., et al. 2022, Topographic Diffusion Revisited: Small Crater Lifetime on the Moon and Implications for Volatile Exploration, *JGRE*, **127**, e2022JE007510
 Fassett, C. I., King, I. R., Nypaver, C. A., & Thomson, B. J. 2018, Temporal Evolution of S-band Circular Polarization Ratios of Kilometer-scale Craters on the Lunar Maria, *JGRE*, **123**, 3133
 Fassett, C. I., & Thomson, B. J. 2014, Crater Degradation on the Lunar Maria: Topographic Diffusion and the Rate of Erosion on the Moon, *JGRE*, **119**, 2255
 Filice, A. L. 1967, Lunar Surface Strength Estimate From Orbiter II Photograph, *Sci.*, **156**, 1486
 Gansler, K., Schmerr, N., Wang, J., et al. 2024, Preparing for Seismic Investigations Using the Inertial Measurement Unit on the Volatiles Investigation Polar Exploration Rover (VIPER) Lunar Mission, *LPSC*, **55**, 1324
 Gertsch, L., Gustafson, R., & Gertsch, R. 2006, Effect of Water Ice Content on Excavatability of Lunar Regolith, in AIP Conf. Proc. 813, SPACE TECH.& APPLIC.INT.FORUM-STAF 2006: 10th Conf Thermophys Applic Microgravity; 23rd Symp. Space Nucl Pwr & Propulsion; 4th Conf Human/Robotic Tech & Nat'l Vision for Space Explor.; 4th Symp. Space Coloniz.; 3rd Symp. on New Frontiers & Future Concepts (Melville, NY: AIP), 1093
 Ghent, R. R., Hayne, P. O., Bandfield, J. L., et al. 2014, Constraints on the Recent Rate of Lunar Ejecta Breakdown and Implications for Crater Ages, *Geo*, **42**, 1059
 Gladstone, G. R., Retherford, K. D., Egan, A. F., et al. 2012, Far-ultraviolet Reflectance Properties of the Moon's Permanently Shadowed Regions, *JGRE*, **117**, E00H04
 Hayne, P. O., Bandfield, J. L., Siegler, M. A., et al. 2017, Global Regolith Thermophysical Properties of the Moon From the Diviner Lunar Radiometer Experiment, *JGRE*, **122**, 2371
 He, R., Sandu, C., Khan, A. K., et al. 2019, Review of Terramechanics Models and Their Applicability to Real-time Applications, *JTerr*, **81**, 3
 He, R., Sandu, C., Mousavi, H., et al. 2020, Updated Standards of the International Society for Terrain-vehicle Systems, *JTerr*, **91**, 185
 Hirabayashi, M., Fassett, C. I., Costello, E. S., & Minton, D. A. 2024, Crater Equilibrium State Characterization Given Crater Production From a Single Power Law, *PSJ*, **5**, 250
 Hörz, F., Basilevsky, A. T., Head, J. W., & Cintala, M. J. 2020, Erosion of Lunar Surface Rocks by Impact Processes: A Synthesis, *P&SS*, **194**, 105105
 Hovland, H. J., & Mitchell, J. K. 1973, Boulder Tracks and Nature of Lunar Soil, *Moon*, **6**, 164
 Hu, W., Li, P., Rogg, A., et al. 2025, A Study Demonstrating That Using Gravitational Offset to Prepare Extraterrestrial Mobility Missions is Misleading, *J. Field Robotics*
 Irani, R. A., Bauer, R. J., & Warkentin, A. 2011, A Dynamic Terramechanic Model for Small Lightweight Vehicles With Rigid Wheels and Grousers Operating in Sandy Soil, *JTerr*, **48**, 307
 Ishigami, G., Miwa, A., Nagatani, K., & Yoshida, K. 2007, Terramechanics-based Model for Steering Maneuver of Planetary Exploration Rovers on Loose Soil, *J. Field Robot.*, **24**, 233
 Ishigami, G., Nagatani, K., & Yoshida, K. 2009, Slope Traversal Controls for Planetary Exploration Rover on Sandy Terrain, *J. Field Robot.*, **26**, 264
 Janosi, Z., & Hanamoto, B. 1961, Analytical Determination of Drawbar Pull as a Function of Slip for Tracked Vehicles in Deformable Soils, in Proc. 1st Int. Conf. on Terrain-vehicle Systems (Torino: Edizioni Minerva Tecnica)
 Jia, Z., Smith, W., & Peng, H. 2012, Terramechanics-based Wheel-terrain Interaction Model and Its Applications to Off-road Wheeled Mobile Robots, *Robot*, **30**, 491
 Kamohara, J., Ares, V., Hurrell, J., et al. 2024, Modeling of Terrain Deformation by a Grouser Wheel for Lunar Rover Simulation, *arXiv:2408.13468*

- Legnemma, K., Brooks, C., & Dubowsky, S. 2004, Visual, Tactile, and Vibration-based Terrain Analysis for Planetary Rovers, in IEEE Aerospace Conf. Proc. 2 (Piscataway, NJ: IEEE), 841
- Li, Y., Basilevsky, A. T., Xie, M., & Ip, W.-H. 2018, Correlations Between Ejecta Boulder Spatial Density of Small Lunar Craters and the Crater Age, *P&SS*, **162**, 52
- Mandt, K. E., Greathouse, T. K., Rutherford, K. D., et al. 2016, LRO-LAMP Detection of Geologically Young Craters Within Lunar Permanently Shaded Regions, *Icar*, **273**, 114
- Metzger, P. T., Anderson, S., & Colaprete, A. 2018, Experiments Indicate Regolith is Looser in the Lunar Polar Regions Than at the Lunar Landing Sites, in Earth and Space 2018: Engineering for Extreme Environments (Reston, VA: ASCE), 79
- Minton, D. A., Fassett, C. I., Hirabayashi, M., Howl, B. A., & Richardson, J. E. 2019, The Equilibrium Size-Frequency Distribution of Small Craters Reveals the Effects of Distal Ejecta on Lunar Landscape Morphology, *Icar*, **326**, 63
- Moore, H. J. 1970, Interagency Report: Astrogeology 22, NASA, <https://ntrs.nasa.gov/api/citations/19700031586/downloads/19700031586.pdf>
- Muller, P., & Savakis, A. 2017, Flowdometry: An Optical Flow and Deep Learning Based Approach to Visual Odometry, in 2017 IEEE Winter Conf. on Applications of Computer Vision (Piscataway, NJ: IEEE), 624
- Nagatani, K., Tachibana, S., Sofne, M., & Tanaka, Y. 2000, Improvement of Odometry for Omnidirectional Vehicle Using Optical Flow Information, in 2000 IEEE/RSJ Int. Conf. on Intelligent Robots and Systems (IROS), 1 (Piscataway, NJ: IEEE), 468
- NASA 2020a, Artemis III Science Definition Report NASA/SP-20205009602, NASA, <https://www.nasa.gov/wp-content/uploads/2015/01/artemis-iii-science-definition-report-12042020c.pdf>
- NASA 2020b, Artemis Plan: NASA's Lunar Exploration Program Overview, NASA, https://www.nasa.gov/wp-content/uploads/2020/12/artemis_plan-20200921.pdf
- Niksirat, P., Daca, A., & Skonieczny, K. 2020, The Effects of Reduced-gravity on Planetary Rover Mobility, *IJRR*, **39**, 797
- Oravec, H. A., Asnani, V., & Zeng, X. 2010, Design and Characterization of GRC-1: A Soil for Lunar Terramechanics Testing in Earth-Ambient Conditions, *JTerr*, **47**, 361
- Pajola, M., Pozzobon, R., Lucchetti, A., et al. 2018, Abundance and Size-frequency Distribution of Boulders in Linne Crater's Ejecta (Moon), *P&SS*, **165**, 99
- Pitcher, C., Komle, N., Leibniz, O., et al. 2016, Investigation of the Properties of Icy Lunar Polar Regolith Simulants, *AdSpR*, **57**, 1197
- Rankin, A., Maimone, M., Biesiadecki, J., et al. 2021, Mars Curiosity Rover Mobility Trends During the First 7 Years, *J. Field Robotics*, **38**, 759
- Sargeant, H. M., Bickel, V. T., Honniball, C. I., et al. 2020, Using Boulder Tracks as a Tool to Understand the Bearing Capacity of Permanently Shadowed Regions of the Moon, *JGRE*, **125**, e2019JE006157
- Schepelmann, A., & Gerdts, S. 2022, Characterization of Infrared Optical Motion Tracking System in NASA's Simulated Lunar Operations (SLOPE) Laboratory, NASA/TM-20220005304, NASA Glenn Research Center
- Shoop, S. 1993, Terrain Characterization for Trafficability 93-6, U.S. Army Corps of Engineers CRREL
- Siegler, M., Paige, D., Williams, J.-P., & Bills, B. 2015, Evolution of Lunar Polar Ice Stability, *Icar*, **255**, 78
- Skonieczny, K., Carbone, T., Whittaker, W. L. R., & Wettergreen, D. S. 2016, Considering the Effects of Gravity When Developing and Field Testing Planetary Excavator Robots, in Field and Service Robotics: Results of the 10th Int. Conf. (Berlin: Springer), 299
- Skonieczny, K., Moreland, S. J., & Wettergreen, D. S. 2012, A Grouser Spacing Equation for Determining Appropriate Geometry of Planetary Rover Wheels, in 2012 IEEE/RSJ Int. Conf. Intell. Robots Syst. 5065 (Piscataway, NJ: IEEE)
- Swamy, V. S., Pandit, R., Yerro, A., et al. 2023, Review of Modeling and Validation Techniques for Tire-Deformable Soil Interactions, *JTerr*, **109**, 73
- Terzaghi, K. 1951, Theoretical Soil Mechanics (London: Chapman and Hall)
- U.S. Army Corps of Engineers 1948, Trafficability of Soils: Laboratory Tests to Determine Effects of Moisture Content and Density Variations: First Supplement 3-240, U.S. Army Engineer Waterways Experiment Station
- Vanga, S., Fassett Caleb, I., Zanetti, M., et al. 2022, Rock Abundance on the Lunar Mare on Surfaces of Different Age: Implications for Regolith Evolution and Thickness, *GeoRL*, **49**, e97610
- Wang, J., Kreslavsky, M. A., Liu, J., et al. 2020, Quantitative Characterization of Impact Crater Materials on the Moon: Changes in Topographic Roughness and Thermophysical Properties With Age, *JGRE*, **125**, e2019JE006091
- Watkins, R. N., Jolliff, B. L., Mistick, K., et al. 2019, Boulder Distributions Around Young, Small Lunar Impact Craters and Implications for Regolith Production Rates and Landing Site Safety, *JGRE*, **124**, 2754
- Wills, B. M. D. 1966, Research Report No. 6, Warren, MIArmy Tank-Automotive Center Land Locomotion Laboratory
- Winkler, E. 1867, Die Lehre von der Elastizität und Festigkeit mit besonderer Rücksicht auf ihre Anwendung in der Technik (Prague: Verlag Dominicus, H.)
- Wong, J. Y. 1980, Data Processing Methodology in the Characterization of the Mechanical Properties of Terrain, *Journal of Terramechanics*, **17**, 13
- Wong, J. Y. 1989, Terramechanics and Off-road Vehicles (Amsterdam: Elsevier)
- Wong, J. Y. 2006, Fundamentals of Terramechanics: Its Applications to the Evaluation of Planetary Rover Mobility, NASA Short Course (Cleveland, OH: NASA Glenn Research Center)